Long Minority-Carrier Diffusion Length and Low Surface-Recombination Velocity in Inorganic Lead-Free CsSnI3 Perovskite Crystal for Solar Cells

Wu, Bo; Zhou, Yuanyuan; Xing, Guichuan; Xu, Qiang; Garces, Hector F.; Solanki, Ankur; Goh, Teck Wee; Padture, Nitin P.; Sum, Tze Chien

2017

Wu, B., Zhou, Y., Xing, G., Xu, Q., Garces, H. F., Solanki, A., et al. (2017). Long Minority-Carrier Diffusion Length and Low Surface-Recombination Velocity in Inorganic Lead-Free CsSnI3 Perovskite Crystal for Solar Cells. Advanced Functional Materials, 27(7), 1604818-.

https://hdl.handle.net/10356/84069

https://doi.org/10.1002/adfm.201604818

DOI: 10.1002/ ((please add manuscript number))
Article type: Full Paper

Long Minority-Carrier Diffusion Length and Low Surface-Recombination Velocity in Inorganic Lead-free $CsSnI_3$ Perovskite Crystal for Solar Cells

Bo Wu, Yuanyuan Zhou, Guichuan Xing, Qiang Xu, Hector F. Garces, Ankur Solanki, Teck Wee Goh, Nitin P. Padture, Tze Chien Sum**

((Optional Dedication))

Dr. B. Wu, Dr. G. Xing, Dr. Q. Xu, Mr. A. Solanki, Mr. T.W. Goh, Prof. T.C. Sum, Division of Physics and Applied Physics, School of Physical and Mathematical Sciences, Nanyang Technological University, 21 Nanyang Link, Singapore 637371

Email: Tzechien@ntu.edu.sg

Dr. Y. Zhou, Mr. H.F. Garces, Prof. N.P. Padture, School of Engineering, Brown University, Providence, RI 02912, USA

Email: nitin_padture@brown.edu

Dr. G. Xing, Institute of Applied Physics and Materials Engineering, Faculty of Science and Technology, University of Macau, Macao SAR, China

Keywords: *Lead-free perovskite crystal, Carrier dynamics, Diffusion length, Surface recombination velocity*

Sn-based perovskites are promising Pb-free photovoltaic materials with an ideal 1.3 eV bandgap. However, to date, Sn-based thin film perovskite solar cells have yielded relatively low power conversion efficiencies (PCEs). This is traced to their poor photophysical properties (*i.e.*, short diffusion lengths (<30 nm) and two orders of magnitude higher defect densities) than Pb-based systems. Herein we reveal that melt-synthesized cesium tin iodide ($CsSnI_3$) ingots containing high quality large single crystal (SC) grains transcend these fundamental limitations. Through detailed optical spectroscopy, we uncover their inherently superior properties, with bulk carrier lifetimes reaching 6.6 ns, doping concentrations of around 4.5×10^{17} cm^{-3}, and minority-carrier diffusion lengths approaching 1 μm, as compared to their polycrystalline counterparts: ~54 ps, >9.2×10^{18} cm^{-3}, and 16 nm, respectively.

$CsSnI_3$ SCs also exhibit very low surface recombination velocity of <2 × 10^3 $cm.s^{-1}$ similar to Pb-based perovskites. Importantly, these key parameters are comparable to high-performance p-type photovoltaic materials (*e.g.*, InP crystals). Our findings predict a PCE of ~23% for optimized $CsSnI_3$ SCs solar cells, highlighting their great potential.

1. Introduction

Perovskite solar cells (PSCs) based on Pb-containing hybrid organic-inorganic perovskites have attracted a great deal of attention, with their power conversion efficiencies (PCEs) skyrocketing to >20% within a few years of development. [1-4] However, the presence of toxic Pb in PSCs has been a concern in the context of their widespread deployment in the future. In particular, hybrid perovskites are prone to decomposition, making the Pb susceptible to leaching into the environment. Thus, inorganic Pb-free (halide, chalcogenide, *etc*) perovskites offer a viable solution to this challenge. [5-9] Elements such as Sn, Bi, and Ge, are less toxic, and they could potentially replace Pb in halide PSCs.[6, 10-15] Specifically, Sn-based perovskite $CsSnI_3$ (with bandgap ~1.3 eV) is a promising candidate for PSCs, with its maximum Shockley-Quiesser PCE limit of ~33%.[16, 17] However, the state-of-the-art PCE of solution-processed $CsSnI_3$ polycrystalline (PC) PSCs without additives is merely 3%,[6, 18] – far below PSCs based on Pb-containing perovskites. This deficiency is attributed to the high density of acceptor defects in $CsSnI_3$, such as Sn or Cs vacancies (V_{Sn} or V_{Cs}), which have very low defect formation energies.[19, 20] This results in a material that is highly *p*-type, with heavily-doped hole concentration as high as 10^{19} cm^{-3}. This is extremely detrimental to solar cell performance because efficient charge extraction and ambipolar charge transport are essential for high performance in PSCs.[6, 21]

The key to realizing the full potential of $CsSnI_3$ for solar cell applications is to develop strategies for reducing the defect density. Improving the crystalline quality through the synthesis such as incorporation of additives (*e.g.*, SnF_2),[6] stoichiometry control,[20] *etc* is one approach. Alternatively, reduction in the number of grain boundaries – the source of high density of surface defects – could also have the same effect. This involves moving to very large-grained polycrystalline thin films or even SCs. In particular, it has been previously demonstrated that $CsSnI_3$ SCs can be fabricated using high-temperature reaction and melting of a stoichiometric mixture of CsI and SnI_2 in evacuated vials.[19, 22] The reduction of the grain boundaries, together with the high-temperature and vacuum-processed synthesis method may yield high-quality $CsSnI_3$ with reduced defects for solar cell applications. Presently, the fundamental properties affecting the solar cell performance of SCs, *e.g.*, doping concentrations, carrier lifetimes/diffusion lengths, surface-recombination velocities (SRVs), *etc.*, are still unknown. Quantifying these properties and establishing a clear photophysical picture of the SCs are paramount for the development of practical $CsSnI_3$ SC solar cells.

Here, ultrafast optical spectroscopy was used, for the first time, to investigate the photophysical properties of $CsSnI_3$ SCs. To preclude any degradation of $CsSnI_3$ in the air (*i.e.*, Sn^{2+} oxidation to Sn^{4+}) that could affect the intrinsic properties,[23] all measurements were performed on melt-synthesized bulk ingots that were inside evacuated Pyrex vials in their as-fabricated condition. The slow-cooled ingots are expected to have single-crystal grains that are hundreds of microns in size, which is of the same order of the beam size used. Thus, all measurements reported here are essentially on $CsSnI_3$ SCs. The SCs show negligible erosion/degradation under repeated laser pulses with highly reproducible properties. Both transient emission and transient reflectance techniques reveal that the photo-excited carriers of the $CsSnI_3$ SCs possess very long bulk carrier lifetime of ~6.6 ns, long minority carrier diffusion length of ~930 nm, and a moderate intrinsic doping concentration of ~4.5×10^{17} cm^{-3}. On the other hand, $CsSnI_3$ polycrystalline thin films (grain size ~100 nm), formed either by solution processing or evaporation exhibit carrier lifetime of ~54 ps, minority-carrier diffusion length of ~16 nm, and a doping concentration of >~9.2×10^{18} cm^{-3}, which is attributed to poor crystalline quality and increased grain boundaries. The $CsSnI_3$ SCs also show negligible surface recombination velocity of <~2×10^3 cm s^{-1}, implying that no further surface passivation (*e.g.*, SnF_2 treatment) is needed. In addition, slow hot-carrier cooling of τ ~1 ps in the $CsSnI_3$ SCs is comparable to Pb-based perovskites.[24, 25] Importantly, solar cell performance simulations using these parameters predict a PCE of around 23% in $CsSnI_3$ SCs solar cells.

2. Results

2.1. Basic characterization and properties

Figure 1a inset shows an as-synthesized $CsSnI_3$ ingot, which has a very smooth surface free of grain boundaries across a large area (>10 × 20 μm^2) as seen in a scanning electron microscope (SEM) micrograph in **Figure S1a** (in Supporting Information (SI)). At room temperature, the 'black' $CsSnI_3$ perovskite exists in the orthorhombic crystal structure (space group *Pnma*).[22] The X-ray diffraction (XRD) pattern of the crushed ingot powders was well-matched to the calculated XRD pattern (**Figure S1b** in SI) of orthorhombic $CsSnI_3$ perovskite. From UV photoelectron spectroscopy (UPS), it was found the valence band edge (VBM) is

~4.72 eV below the vacuum level and the Fermi-level is only 0.16 eV above the VBM, confirming it is a p-type semiconductor (**Figure S2**).

2.2. **Photoluminescence Properties**

Figure 1a shows the $CsSnI_3$ SC photoluminescence (PL) spectra with one-photon (400 nm, 700 nm, 800 nm) and two-photon (1350 nm) excitations. The PL spectra are centered at 950 nm (1.31 eV) with one-photon excitation, but red-shift to 990 nm (1.25 eV) with two- photon excitation. This red-shift can be attributed to PL re-absorption effect (*e.g.*, high subgap absorption from tail states; small Stokes shift),[26, 27] and also to a smaller bandgap in the bulk crystal due to reduced lattice strain.[28-30]

Figure 1b summarizes the carrier-concentration dependent time-resolved PL (TRPL) data for $CsSnI_3$ SC. The PL intensity just after excitation (t = 0) can be used to evaluate the emission species in halide perovskite systems.[31] Briefly, for emission dominated by free-carrier bimolecular recombination; the initial PL intensity exhibits a quadratic dependence with the photoexcited carrier concentration: $I_{PL|t=0} \propto n_0^2$, where n_0 is the photoexcited carrier density; the effective carrier lifetime drops as intensity increases. For emission dominated by photoexcited carriers with doped carriers, the initial PL intensity exhibits a linear dependence with the photoexcited carrier concentration: $I_{PL|t=0} \propto n_0 p_0$,where p_0 is the doped carrier concentration (or defect density); the effective carrier lifetime remains constant until all the doped carriers have recombined. It was found that the PL intensity following excitation increases linearly with carrier concentration in the low-density regime (carrier concentration $N_c < 4 \times 10^{17}$ cm^{-3}), whereas it has a nearly-quadratic dependence in the high density regime ($N_c > 5 \times 10^{17}$ cm^{-3}). Meanwhile, the effective PL lifetime also starts to drop under similar carrier concentrations. Such behavior corresponds to the recombination of excess minority carriers with unintentionally doped majority carriers or *via* mid-gap deep traps under weak excitation and bimolecular recombination of excess free carrier under intense excitation.[31] In the $CsSnI_3$ system, the dominant point defect is V_{Sn} due to its low defect formation energy, which is a shallow native defect rendering $CsSnI_3$ an intrinsic *p*-type semiconductor.[19] First-order recombination in the $CsSnI_3$ system occurs mainly in the case of excess electrons (minority carriers) recombining with the doped holes. Hence, from this we estimate an intrinsic doped hole concentration of ~4-5 × 10^{17} cm^{-3}, consistent with a previous report.[19] Although some variations exist in samples from batch to batch, a general doping concentration of the order 10^{17} cm^{-3} can be consistently found for $CsSnI_3$ SCs. This value is higher, or almost comparable, to that of the widely studied $MAPbI_3$ polycrystalline thin films (with typical values of 10^{15} - 10^{17} cm^{-3}).[31-33]

Comparative experiments were also performed on $CsSnI_3$ polycrystalline thin films sealed in vacuum. Their lifetimes start to decrease at a carrier concentration of ~0.92×10^{19} cm^{-3}. Simultaneously, the recombination order increases from first-order to higher order when Auger recombination and amplified stimulation emission (ASE) occur. These results clearly show that the thin film is heavily doped by intrinsic defects. The defect density also agrees very well with previous reports (*i.e.*, doped carrier concentration on the order of 10^{19} cm^{-3} (**Figure S3** in SI)).[6, 21] Generally, the thin films gave weak PL signal. Hence, we measured their PL from relatively brighter regions in an effort to obtain better signal-to-noise for the streak camera. This implies that the typical average doped carrier concentration in these thin films should be >0.92×10^{19} cm^{-3}. Such heavy intrinsic doping would greatly reduce the minority carrier mobilities and lifetimes, thus limiting the PSC performance.

To investigate the excitation-wavelength dependent PL dynamics in $CsSnI_3$ SCs, we kept the photoexcited carrier concentrations to <4×10^{17} cm^{-3} to ensure dominant first-order recombination kinetics. Several wavelengths were chosen: 400 nm, 700 nm, and 800 nm for one-photon and 1350 nm for two-photon excitations. The pseudo-color images of the TRPL profiles are shown in **Figure 1c,** where a clear lifetime lengthening with increasing excitation wavelengths is evident. These decay transients at the ~950 nm emission were globally-fitted (discussed later) as shown in **Figure 1d**. The PL decay using two-photon excitation shows a dominant single-exponential decay with a time constant of 6.6±0.1 ns. Given that two-photon excitation usually has a penetration depth on the order of 100 μm,[34] its PL decay lifetime can, therefore, be attributed to the bulk carrier lifetime. In contrast, the carrier lifetimes of solution-processed $CsSnI_3$ thin films ranges from 40-50 ps (*i.e.*, from TRPL and transient absorption (TA)), which is two orders of magnitude lower than the bulk lifetimes from $CsSnI_3$ SCs (**Figure** S3**, S4** in SI). To exclude any possible influence from effects such as inadvertent impurities incorporation from the solution-processing, we also prepared polycrystalline thin films by evaporating $CsSnI_3$ ingots in vacuum onto substrates. Consistently short lifetimes were also found for these evaporated thin films (**Figure S5** in SI). A direct conclusion is the greatly improved carrier lifetimes in $CsSnI_3$ SCs, which is attributed to the elimination of grain boundaries and surface defects. The high crystalline quality obtained using these high-temperature melting method significantly reduced the intrinsic defects, which will be discussed in greater detail later. On the other hand, the dynamics of the $CsSnI_3$ SC PL emission from one-photon excitation is not only due to bulk carrier recombination, but is also related to carrier diffusion and surface recombination, which accelerate the PL decay dynamics. As shown in **Figure 1c**, with highly-absorbing excitation wavelengths (*e.g.*, 400 nm), the effect from surface carrier diffusion and recombination is more severe than weakly - absorbing excitation wavelengths (*e.g.*, 800 nm). A model based on one-dimensional diffusion is used to reproduce/simulate these processes:[35, 36]

$$\frac{N(x,t)}{t} = D\frac{{}^{2}N(x,t)}{x^{2}} \quad \frac{N(x,t)}{}, \tag{1}$$

where N is the carrier concentration, D is the diffusion coefficient, and τ is the carrier lifetime, x is the axis along the light propagation direction. Surface recombination occurs at the boundary with a velocity S:

$$\begin{aligned} &N(0,t) = \frac{D}{S}\frac{\partial N(x,t)}{\partial x}\bigg|_{x=0}, N(L,t) = 0, \\ &N(x,0) = N_0 \exp(-\alpha x). \end{aligned} \tag{2}$$

where L is the thickness of the crystal, α is the excitation light absorption coefficient, N_0 is the carrier concentration at t=0 and x=0. Applying the boundary conditions, the analytical solution of equation (1) is:

$$\begin{aligned} &N(x,t) = \frac{N_0}{2}\exp(\frac{-t}{\tau_{\mathrm{R}}})\exp(-\frac{x^2}{4Dt}) \\ &\times[W(\alpha\sqrt{Dt} - \frac{x}{2\sqrt{Dt}}) - \frac{S+\alpha D}{S-\alpha D}W(\alpha\sqrt{Dt} + \frac{x}{2\sqrt{Dt}}) + \frac{2S}{S-\alpha D}W(S\sqrt{\frac{t}{D}} + \frac{x}{2\sqrt{Dt}})] \end{aligned}, \tag{3}$$

where τ_{R} is the bulk carrier lifetime and $W(x) = \exp(x^2)\mathrm{erfc}(x)$.

The collected PL from the crystal (after factoring over the 4π total solid angle) can be expressed as:

$$I_{\mathrm{PL}}(t) = A\int_{0}^{x=L}\int_{0}^{\theta=\theta_0} N(t,x)\exp(-\alpha_{\mathrm{PL}}\frac{x}{\cos\theta})2\pi\sin\theta d\theta dx, \tag{4}$$

where A is proportional to PL collection efficiency, α_{PL} is the absorption coefficient at the emission wavelength, L is the thickness of the SC, θ is the colatitude in spherical coordinates with zenith direction along the collection line direction. θ_0 is the half apex angle of the light emitting cone that can be collected by the lens. In our measurement θ_0 is ~ 14°, resulting in a near-unity of the $\cos\theta$, hence the equation can be approximated to one-dimensional. The collected PL dynamics depend on the carrier diffusion coefficient D, surface recombination velocity S, as well as the excitation/emission light absorption coefficients.

Different wavelength one-photon excitations alter the carrier distribution profiles as shown in Eq. 3 due to the change in the absorption coefficients (α) and hence modify the PL dynamics in Eq. 4. The diffusion coefficient (D) and surface recombination velocity (S) can be extracted by global fitting the PL dynamics under different wavelength one-photon excitations. The global fitting of the PL dynamics under three different excitation wavelengths (400 nm, 700 nm and 800 nm) with distinct absorption coefficients ensures the fitted values of the shared parameters (D and S) are obtained with a high coefficient of determination (R-squared value: 0.9819). The fits revealed that D can be as large as 1.3±0.1 cm^2s^{-1}. Since the recombination (~10^{17} cm^{-3}) is mainly from photo-generated minority carriers with the doped carriers, the diffusion coefficient D is attributed to the minority carriers (electron), rendering a high minority-carrier mobility of ~50 cm^2 V^{-1} s^{-1} at room temperature. The high minority carrier mobility, together with the long carrier lifetime, indicates that the minority carriers possess high diffusion capability. The contribution from surface recombination is rather small, with a SRV of $1.8\pm0.4 \times 10^3$ cm s^{-1}. Such small SRV is comparable, or superior to the best values reported for semiconducting crystals such as Ge,[37] InP,[38] $MAPbBr_3$,[39] and $MAPbI_3$.[34] The small contribution of the SRV to the carrier dynamics indicates that surface passivation is not necessary for $CsSnI_3$ SCs for solar cells or photodetector applications.

2.3. **Transient Reflectance Spectroscopy**

To further investigate the carrier dynamics and the non-radiative processes, we also performed transient reflectance (TR) spectroscopy (or TA under reflection geometry) on the $CsSnI_3$ SCs, and correlated the findings with the PL studies. **Figures 2a** and **2b** show pseudo-color TR profiles of $CsSnI_3$ SCs with 400 nm and 800 nm excitations. TR profiles with other excitation energies can be found in SI (**Figure S6**). The transient profiles in **Figure 2c** show typical anti-symmetric peaks near the band-edge, similar to previous reports for $MAPbBr_3$ and $MAPbI_3$ crystals.[26, 39] Halide perovskites have large refractive indices (*i.e.*, n ~3 for $CsSnI_3$) in the visible to near infrared (VIS-NIR) region (**Figure S7** in SI). Thus, the TR signal is dominated by the refractive index change (Δn) resulting from photoexcited state-filling.[24, 39] A detailed interpretation of the TR profile relies on the exact decomposition of the free carrier absorption, trap-state absorption, *etc.*, which are still unknown. In our simple model, $CsSnI_3$ is treated as a direct bandgap semiconductor with near-band-edge absorption coefficient satisfying $\alpha \propto \sqrt{E-E_g}$, where E_g is the bandgap. The refractive index change (Δn) can be calculated using the Kramers-Kronig relations: $\Delta n(\omega)=\frac{c}{\pi}P\int_0^\infty \frac{\Delta\alpha(\omega)}{\omega'^2-\omega^2}d\omega'$, where c is the speed of light in vacuum, P is the Cauchy principal value of the integral, $\Delta\alpha$ is the absorption coefficient change [40] We could satisfactorily reproduce the transient reflectance profile near the band-edge (and up to ~1050 nm) using E_g ~ 1.33 eV and the *n*-*k* data obtained from ellipsometry for a $CsSnI_3$ thin film (Figure S7 in SI). The fitting results only start to deviate from the experimental results at around 1100 nm due to the presence of strong sub-bandgap states bleaching, which we did not take into account (Figure S6 in SI). The isobestic point between the two anti-symmetric peaks basically reflects the average absorption position of the excited carriers, therefore, the dynamic change of the isobestic point position corresponds to the energy position of the hot carriers. Before reaching a stable transient reflection profile at ~10^2 ps, we observe a continuous red-shift of the peaks and the isobestic point within a few ps. This corresponds to the 'hot-carrier' relaxation process in perovskite SCs.[24, 25] In addition, for high energy photo-excitation (*e.g.*, 400 nm, 500 nm pumping), a clear +ΔR region can be seen in the ultrafast time scale (<1 ps) just below the band-edge (**Figures 2a, 2d** and Figure S6 in SI). As shown in **Figure 2d**, the TR profile (with 400 nm excitation at 300 fs delay) at ultra-short timescale is completely different from the TR profiles at later delay times (**Figure 2c**). We attribute this behavior to arise from the interplay between the hot-carrier effects and the bandgap renormalization (BGR). Due to BGR after excitation, the bandgap is shifted to lower energy. High energy photo-excitation yields hot-carriers with high temperature, and as a result, the newly formed band-edge due to BGR will be less occupied compared to one at thermal equilibrium. This leads to the formation of a photo-induced absorption (PIA) band below the bandgap that alters the shape of the TR profile.[24] We find that the best fit of the TR profile at 300 fs with 400 nm excitation at a fluence of ~2 μJ cm^{-2} gave a carrier temperature of ~1800 K and a bandgap shift of ΔE = 0.1 eV.

After accounting for the spectral origins in TR spectra profiles, we next examine the TR kinetics. First, the rise time of the band-edge TR signal is important as it corresponds to the relaxation of the hot-carriers to the band-edge. As shown in **Figure 2e**, the rise time monitored at ~920 nm increases with higher energy photo-excitation. For example, with 400 nm high energy photo-excitation, the rise time is ~1 ps, indicating that the hot-carriers created by 400 nm excitation require ~1 ps to relax to the band-edge. Using D = 1.3 cm^2 s^{-1}, the hot carriers can diffuse as far as ~11 nm before relaxation, which is close to the absorption length of 400 nm excitation light (~50 nm). This also demonstrates the feasibility of harvesting hot-carriers from $CsSnI_3$ SCs.[41, 42]

The decay of the TR signal signify the relaxation of carriers to the ground state. Due to the abrupt change of refractive index at the air (or glass)/perovskite interface, the TR signal is dominated by contributions from the surface region within a few nm.[43, 44] Hence, the carrier-induced reflectivity change could be evaluated by $N(0,t)$ in Eq. 1-3:

$$N(t) = N_0 \exp(\frac{-t}{\tau_R}) \times [\frac{S}{S-\alpha D} W(S\sqrt{\frac{t}{D}}) - \frac{\alpha D}{S-\alpha D} W(\alpha\sqrt{Dt})]. \quad (5)$$

After the relaxation of hot-carriers, the dominating TR decay mechanism is carrier diffusion and surface/bulk recombination. The excitation intensity is set as low as possible (typically ~μJ cm^{-2}) to minimize any higher-order recombination. Negligible intensity-dependence of the decay dynamics can be observed (**Figure S8** in SI) under the fluence regime we measured, indicating that the recombination is dominated by that between the minority carriers and the doped carriers. Hence, the measured diffusion is mainly from the minority carriers. This is similar to the findings from PL emission dynamics where faster TR decay is observed when highly absorbing excitation photons are used. As shown in **Figure 2f**, global-fitting of the TR decay data obtained from four different excitation wavelengths (400 nm, 600 nm, 700 nm, and 800 nm) yielded a diffusion coefficient D of 1.9±0.1 $cm^2\ s^{-1}$, which is comparable to that determined from PL fittings. The contribution from surface recombination is also much smaller than that from diffusion, i.e., $S << \alpha D$, which makes it challenging to determine the exact value of the SRV. A high fitting uncertainty of S=0.8±1.2 × 10^3 cm s^{-1} was therefore obtained. Correlating with the earlier PL results, we believe that the acceptable value of the SRV in the $CsSnI_3$ SC is <2 × 10^3 cm s^{-1}. The low SRV leads to a $\Delta R/R$ recovery that is dominated by carrier diffusion (the second term in the square brackets in Eq. 5), rather than surface recombination (the first term in the square brackets in Eq. 5). The simulated carrier distribution profiles after photoexcitation by 400 nm and 800 nm photons are shown in **Figure 2g** and **2h**, respectively. The 400 nm excitation creates a high concentration of carriers in the shallower regions, which leads to more significant carrier diffusion compared to the 800 nm excitation.

3. Discussion.

Carrier transport and recombination are greatly influenced by the intrinsic point defects (vacancies, interstitials, anti-sites), line defects (dislocation), surface defects (free surface, grain boundaries), *etc*. SRV is therefore a very important parameter signifying the quality of a

SC's surface and polycrystalline grain boundaries. Surface recombination is commonly attributed to the recombination from dangling bonds created deep surface defects and from impurities at the surface.[45] Based on the Shockley-Read-Hall (SRH) type recombination model, these defects/impurity levels should be most efficient in capturing both electrons and holes when they are located at the middle of the bandgap, resulting in the highest SRV. Low SRV semiconductors such as InP (10^2 cm s^{-1}) 22 and $MAPbBr_3$ (10^3 cm s^{-1}) [34, 39] and high SRV semiconductors such as GaAs and CdTe (> 10^5 cm s^{-1}) [46, 47] are not only dependent on their crystal qualities but also the position of their surface defect with respect to their energy bands. High crystalline quality indicates low defect densities in the bulk and at the surface – the latter determines the SRV. Using $S=\sigma v_{th}N_t$, where v_{th} is the carrier thermal velocity (~ 2 × 10^7 cm s^{-1}), σ (~10^{-15} cm^2) is a typical recombination surface cross section in semiconductors and N_t is surface trap density,[48] we estimate a surface trap density of < 10^{11} cm^{-2}, comparable to that of $MAPbI_3$ thin films (~5 × 10^{11} cm^{-2}).[49] In addition, we also performed density functional theory (DFT) calculations on the electronic band structure of the bulk $CsSnI_3$ SC and the (001) surfaces. We found that the (001) surfaces terminated with either CsI or SnI will not introduce any surface states within the bandgap (**Figure S9** in SI), which may explain why the SRV in the high-quality $CsSnI_3$ single crystals can be so low (< 2 × 10^3 cm s^{-1}).

Carrier mobilities are determined by the average time between scattering processes. These processes include the scattering by crystal defects/ionized impurities and by phonons. Carrier lifetime is greatly influenced by deep-level defects, which provide recombination centers. For intrinsically-doped materials, the minority-carrier transport can be significantly impaired due to the presence of high amounts of donor or acceptor defects. This is undeniably the case for the $CsSnI_3$ polycrystalline thin films, where an intrinsic-doped carrier concentration as high as 0.92 × 10^{19} cm^{-3} was found. This high density of intrinsic defects renders it a heavily doped *p*-type material. The minority carrier diffusion length can be estimated by measuring PL quenching with an efficient electron extraction layer (*e.g.*, $PC_{61}BM$) as described previously.[50] Both methods of (i) depositing an efficient charge extraction layer to measure the carrier diffusion coefficient in thin films and (ii) using wavelength-dependent excitation to measure that in thick single crystals are well-established techniques based on 1D diffusion model. The diffusion coefficients measured by both techniques are comparable as shown for $MAPbBr_3$ single crystals, [34, 39] which are also comparable to the results using electrical techniques such as Hall effect and time-of-flight measurements.[51, 52] The PL lifetime drops slightly from 54.2 ps to 47.8 ps (**Figure S10** in SI). Assuming highly efficient electron extraction at the heterojunction, the decrease of PL lifetime corresponds to a minority-carrier mobility of ~1.8 $cm^2\ V^{-1}\ s^{-1}$, and a minority-carrier diffusion length of only ~16 nm. The polycrystalline thin-film carrier-diffusion lengths are comparable to a previous report for another Sn-based hybrid perovskite ($CH_3NH_3SnI_3$, ~30 nm thickness), and it is responsible for the poor PSC performance obtained with polycrystalline thin films.[11]

Unlike the polycrystalline case, the minority-carrier diffusion properties in $CsSnI_3$ SCs are greatly improved. Based on our above results, we estimate a diffusion length of the minority carriers (electrons) of around 930 ± 70 nm using $L=\sqrt{D\tau}$, where D is the diffusion coefficient and τ is the carrier lifetime. The minority carrier diffusion length is much higher than that of the absorption thickness (*i.e.*, ~300 nm near the 900 nm band-edge), and is comparable to that of the Pb-based perovskites.[50, 53] For more direct comparison with other *p*-type solar cells materials, **Table 1** shows *p*-type InP with similar direct bandgap (1.35 eV) possesses a diffusion coefficient of 5 $cm^2\ s^{-1}$, doping level of 4-5 × 10^{16} cm^{-3}, lifetime of $\tau = 4$ ns, and a comparable low SRV of 500 cm s^{-1}.[38] Given that the best InP based solar cells have a reported PCE up to 22%,[54, 55] it is, therefore, entirely feasible to obtain high PCE $CsSnI_3$ SCs-based solar cells.

To correlate our findings to solar cell performance, we simulate the relation between surface recombination, grain size, and PCE. The PCE are optimized values in which we assume the solar cells have optimized energy level alignments, Ohmic contacts, and efficient charge extraction by electrodes. Detailed procedures are elaborated in the Methods section and SI. The effective carrier lifetime is determined by the grain-size (d), diffusion coefficient (D), and surface recombination velocity (S):[39, 56]

$$\frac{1}{\tau_{\text{eff}}}=\frac{1}{\tau_{\text{B}}}+\frac{1}{\dfrac{d}{2S}+\dfrac{1}{D}\left(\dfrac{d}{\pi}\right)^2}, \tag{6}$$

In the equation, we assumed that the crystalline quality is not varying with grain size and that the grain boundaries in the polycrystalline films are the same as that of our single crystals, *i.e.*, possessing the same concentration of recombination centers per unit area and capture cross sections *etc*. The grain size-dependent effective carrier lifetimes with selected SRVs (10^2, 10^3,10^4,10^5 cm s^{-1}) are shown in **Figure 3a**. Upon shrinking the size of the grains from SC to small dimensions, there is a drastic drop in the lifetimes. Nonetheless, using the τ_B and S values obtained experimentally from our melt-synthesized $CsSnI_3$ SCs, we determined an effective lifetime of ~3 ns for 300 nm size grains, which is much longer than the measured value of around 50 ps. This indicates that the crystallinity of the polycrystalline thin films is much worse than that of SC, resulting in much higher *S* at the grain boundaries and lower bulk lifetime τ_B; this deviation from the effective lifetime trend is obtained from Eq. 6. Even for the evaporated thin films, the crystalline quality of the single crystal is not preserved during the evaporation process. Another possible reason is the grain-boundaries of polycrystalline $CsSnI_3$ cannot be treated equivalent to that of single crystal surface: the former provides much more deep-defects (resulting from disorder/misorientation, unintentional impurities incorporation, fast degradation, stoichiometry deviations, *etc.*) that accelerate the grain-boundary recombination. Previously, we found that for solution-processed $CsSnI_3$ polycrystalline thin films, the emission lifetime increases from ~70 ps without any additives to ~1.4 ns with SnF_2 additive.[57] In that earlier study, it was suggested that the SnF_2 addition optimized the crystallization process and reduced the defect density.

To gain deeper insights into the relations between grain-size, SRV, and PSC performance, we fixed the bulk carrier lifetime value obtained from SC (~6 ns), and plotted a pseudo-color map of the PCE with varying grain-sizes and SRV as shown in **Figure 3b**. Theoretically, 23% PCE can be obtained using $CsSnI_3$ SCs or large-grained polycrystalline thin films under optimized conditions. The size-dependent PCE, short-circuit current density (J_{SC}), fill factor (FF), and open-circuit voltage (V_{OC}) using the bulk lifetime and SRV from SCs are shown in **Figure 3c**. As a comparison, we also presented the performance with non-optimized parameters from polycrystalline $CsSnI_3$ without SnF_2 addition. We first assumed that $1/\tau_B$ and *S* scale by the same factor when translating from optimized SC fabrication conditions (with higher crystalline quality) to the non-optimized thin-film fabrication conditions (with poorer crystalline quality) (*i.e.*, increased defect density both at the grain boundary and in the bulk crystal). The scaling factor is around 10^2 (calculated using Eq. 6), which is consistent with the approximately 2 orders of magnitude increase in defect density in SC compared to polycrystalline thin film. The simulated device performance with these increased *S* and $1/\tau_B$ is shown in Figure 3c, which is consistent with our recent experimental results (solid circles).[5] The simulated V_{OC} and FF is higher than the experimental results as the simulation is based on ideal and optimized conditions. The grain-size-dependent J_{SC} is slightly lower than the reported value, possibly due to a passivation of the defects at the interfaces by the charge transport layers in a real device. Hence, replacement of polycrystalline thin films with the high-temperature synthesized SCs would allow larger improvements to the performance of $CsSnI_3$-based PSCs. It is important to note that the predicted 23% PCE need not be the ultimate upper limit for $CsSnI_3$ SCs. Usually, moderate doping concentration and high quality materials (with as few as possible deep-level defects) are needed to obtain maximum device efficiency, *e.g.*, in Si-based solar cells, the optimized carrier concentration is ~10^{16} cm^{-3}.[58] The intrinsic doping concentration and deep-level defects formation in $CsSnI_3$ SCs can be further optimized with judicious chemical tuning (*e.g.*, adding SnF_2, modifying stoichiometry, optimizing synthesis methods, *etc*.) or physical tuning (*e.g.*, ion implantation, ion diffusion, annealing, *etc*.) of the doping concentration. Currently, fabricating solar cells using these $CsSnI_3$ ingots is still very challenging: the critical step is to precisely control the thickness of the single crystals to be comparable to the carrier diffusion length (~ 1 μm). This requires new technique developments in perovskite single crystal slicing, polishing as well as other growing methods typical for monocrystalline inorganic semiconductors (*e.g.*, molecular beam epitaxy). We foresee there will a great of leap of the performance once the new methods of fabricating high-quality and thin $CsSnI_3$ single crystals are grasped. Furthermore, the stability of $CsSnI_3$ SCs is still far from satisfactory. Under ambient conditions (20°C, 60% humidity, continuous illumination), the PL is quenched within 2 hours (**Figure S11** in SI). Comparatively, the stability is better for SCs than thin films. Nonetheless, we envisage that such stability issues will be gradually mitigated as the field progresses, just like in the case of $MAPbI_3$.

4. Conclusion

With ultrafast optical spectroscopies, we uncovered that melt-synthesized $CsSnI_3$ ingots show exceptional photophysical properties as active layer material for PV application.The minority carriers possess a diffusion length approaching 1 μm, which is much longer than the absorption length and greatly improved compared to polycrystalline thin films of around 16 nm. We interpret these as a consequence of reduced grain boundaries and improved crystalline quality that lead to much lower defect densities, higher minority carrier mobility and lifetime. The SRV is very low ($<2 \times 10^3$ cm s^{-1}) contributing negligibly to the photophysical dynamics, which indicates the ingots do not need any surface passivation to achieve optimal performance. Thus, these findings indicate that replacing polycrystalline thin films with melt-synthesized ingots is expected to provide a performance leap for $CsSnI_3$-based solar cells.

5. Experimental Section

Crystal Synthesis and Characterization: The synthesis of $CsSnI_3$ perovskite ingot containing large single crystal grains follows a similar procedure that is reported elsewhere.[13, 57] Stoichiometric amounts of SnI_2 (Alfa, USA) and CsI (Sigma-Ardrich, USA) were mixed and placed in pyrex vials (~3 mm diameter). The vials were then evacuated to 5×10^{-6} Torr vacuum for 9 h and sealed using a oxy-methane torch. The evacuated vials were then placed in a tube furnace and heated to 550 ˚C (above the melting point of $CsSnI_3$ perovskite of 435 ˚C) and held for 26 min, followed by slow cooling at a rate of 0.04 $˚C.min^{-1}$ to room temperature. For scanning electron microscope (SEM; LEO 1530VP, Carl Zeiss, Munich, Germany) observation, the vial was broken and the $CsSnI_3$ ingot sample was quickly transferred to the SEM chamber and evacuated. For X-ray diffraction (XRD) characterization, the vial was broken inside a N_2-filled glovebox, and the ingot was crushed into a powder. The powder was spread onto a holder and sealed with an X-ray transparent polymer film. The sample was removed from the glovebox and XRD (Bruker D8-advance, Karlsruhe, Germany) was performed in air using Cu K_α radiation and the following parameters: 2θ range 10˚ to 60˚, 0.02˚ step scan. The resulting XRD pattern was indexed with the help of the PDF2 database. The stimulated XRD experiment is performed using the PowderCell 2.3 software based on a stoichiometric $CsSnI_3$ orthorhombic crystal model; instrumental broadening is considered in this model. The polycrystalline thin films of $CsSnI_3$ perovskite were deposited using two different methods – solution processing and evaporation – on glass substrates inside a N_2-filled glovebox or under high-vacuum condition (10^{-5} Pa). The films are then sealed before removing them into the ambient for further characterization.

TIPL and TRPL: Time-integrated photoluminescence (TIPL) measurements were conducted by directing the excitation laser pulses onto the ingots/thin films. The PL was collected at a backscattering angle by a spectrometer (Acton, Spectra Pro 2500i) and CCD (Princeton Instruments, Pixis 400B). Time-resolved photoluminescence (TRPL) was collected using an Optronis Optoscope^{TM} streak camera system which has an ultimate temporal resolution of 6 ps.

TR Spectroscopy: Transient Reflectance (TR) measurements were performed using a commercial non-degenerate Helios^{TM} (Ultrafast Systems LLC) pump-probe setup in reflection geometry. Both the pump and probe beams have a very small incident angle (<10˚) in the TR measurement. The pump pulses were generated from an optical parametric amplifier (Light Conversion TOPAS^{TM}) that was pumped by a 1-kHz regenerative amplifier (Coherent Legend^{TM}, 800 nm, 150 fs, 1 mJ). A mode-locked Ti-sapphire oscillator (Coherent Vitesse, 80MHz) was used to seed the amplifier. The probe pulses were a white light continuum generated by passing the 800 nm fs pulses through either a 2 mm sapphire plate for visible part (400 nm – 800 nm) or a 1 cm sapphire plate for NIR part (800 nm – 1600 nm). The probe light was collected using a CMOS sensor for UV-VIS part and InGaAs diode array sensor for NIR part. To improve the signal to noise ratio, the same sensor was used to collect the probe light before the sample as a reference.

Device Simulation: The short-circuit current density (J_{SC}), open-circuit voltage (V_{OC}) and fill factor (FF) determine the output power-conversion efficiency: PCE = ($J_{SC} \times V_{OC} \times$ FF)/P_{in}, where P_{in} is the input power (=100 mW cm^{-2} for 'one-sun' conditions). We simulated the optimized device performance. Part of the simulation was performed in a similar manner to that in a previous report as illustrated below.[59] The V_{oc} can be expressed as:[60]

$$V_{OC} = \frac{nkT}{q}\ln\left(\frac{J_{SC}}{J_0}\right), \tag{6}$$

where n is the ideal factor determined by the recombination type, kT/q is the thermal energy, J_0 is the reverse saturation current density in the dark. The dark current is expressed as:

$$J_{d} = J_{od}\exp(\lambda_{d}V - 1) + J_{or}\exp(\lambda_{r}V - 1) \tag{7}$$

where $\lambda_{d} = q/kT, \lambda_{r} = q/2kT$. $J_{od} = qD_{p}p_{n0}/L_{p} + qD_{n}n_{p0}/L_{n}$ is the diffusion induced reverse saturation current density and $J_{od} = qn_{i}W/2\tau_{eff}$ is the recombination induced reverse saturation current density. $D_{p,n}$ and $L_{p,n}$ are the diffusion coefficients and diffusion lengths for holes and electrons, respectively. W is the depletion width of ~50 nm using the effective mass of electrons and holes of 0.16 m_0 and 0.07 m_0, respectively.[23] We found that the latter contribution dominates for $CsSnI_3$ in our case. For optimized solar cell, the FF is related to the V_{OC}:[61]

$$\mathrm{FF} = \frac{\frac{V_{OC}}{nkT/q} - \ln\left(\frac{V_{OC}}{nkT/q} + 0.72\right)}{\frac{V_{OC}}{nkT/q} + 1}. \tag{8}$$

For J_{SC}, it was previously treated as a constant assuming that the strong build-in field can extract all the photogenerated charges under short-circuit condition for optimized $MAPbI_3$ devices. However, for $CsSnI_3$, the diffusion lengths under poorer working conditions do not necessarily result in the extraction of all the charges. Hence, we use J_{SC}=J_{drift}+$J_{diffuse}$ to calculate the charge extraction efficiency, where the first term on the right side accounts for the current originating from minority carrier drift in the depletion region and the second term accounts for carrier diffusion out of the depletion region. For good working conditions such as shown in the main text for vacuum-processed single crystals, the J_{SC} is approximately a constant, while using parameters from polycrystalline thin films without additives; the J_{SC} varies significantly for small grain size. Further details of the calculations are provided in SI.

Supporting Information
Supporting Information is available from the Wiley Online Library or from the author.

Acknowledgements
B. Wu and Y. Zhou contributed equally to this work. The work received financial support from Nanyang Technological University start-up grant M4080514; the Ministry of Education Academic Research Fund Tier 1 grant RG101/15, and Tier 2 grants MOE2014-T2-1-044 and MOE2015-T2-2-015; and from the Singapore National Research Foundation through the Singapore–Berkeley Research Initiative for Sustainable Energy (SinBeRISE) CREATE Program and the Competitive Research Program NRF-CRP14-2014-03 is gratefully acknowledged. Y. Zhou, H.F. Garces, and N.P. Padture are grateful to the US National Science Foundation (award nos. DMR-1303913, OIA-1538893) for the financial support.

Received: ((will be filled in by the editorial staff))
Revised: ((will be filled in by the editorial staff))
Published online: ((will be filled in by the editorial staff))

References

[1] A. Kojima, K. Teshima, Y. Shirai, T. Miyasaka, *J. Amer. Chem. Soc.* **2009**, *131*, 6050-6051.
[2] H.-S. Kim, C.-R. Lee, J.-H. Im, K.-B. Lee, T. Moehl, A. Marchioro, S.-J. Moon, R. Humphry-Baker, J.-H. Yum, J. E. Moser, M. Graetzel, N.-G. Park, *Sci. Rep.* **2012**, *2,* 591.
[3] M. M. Lee, J. Teuscher, T. Miyasaka, T. N. Murakami, H. J. Snaith, *Science* **2012**, *338*, 643-647.
[4] W. S. Yang, J. H. Noh, N. J. Jeon, Y. C. Kim, S. Ryu, J. Seo, S. I. Seok, *Science* **2015**, *348*, 1234-1237.
[5] N. Wang, Y. Zhou, M. Ju, H. F. Garces, t. Ding, S. Pang, X. Zeng, N. P. Padture, X. Sun, *Adv. Energy Mater.*, DOI: 10.1002/aenm.201601130.
[6] M. H. Kumar, S. Dharani, W. L. Leong, P. P. Boix, R. R. Prabhakar, T. Baikie, C. Shi, H. Ding, R. Ramesh, M. Asta, M. Graetzel, S. G. Mhaisalkar, N. Mathews, *Adv. Mater.* **2014**, *26*, 7122-7127.
[7] W. W. Meng, B. Saparov, F. Hong, J. B. Wang, D. B. Mitzi, Y. F. Yan, *Chem. Mater.* **2016**, *28*, 821-829.
[8] Y. Y. Sun, M. L. Agiorgousis, P. H. Zhang, S. B. Zhang, *Nano Lett.* **2015**, *15*, 581-585.
[9] S. Perera, H. L. Hui, C. Zhao, H. T. Xue, F. Sun, C. H. Deng, N. Gross, C. Milleville, X. H. Xu, D. F. Watson, B. Weinstein, Y. Y. Sun, S. B. Zhang, H. Zeng, *Nano Energy* 2016, 22, 129-135.

[10] F. Hao, C. C. Stoumpos, D. H. Cao, R. P. H. Chang, M. G. Kanatzidis, *Nat.Photon.* **2014**, *8*, 489-494.
[11] N. K. Noel, S. D. Stranks, A. Abate, C. Wehrenfennig, S. Guarnera, A. A. Haghighirad, A. Sadhanala, G. E. Eperon, S. K. Pathak, M. B. Johnston, A. Petrozza, L. M. Herz, H. J. Snaith, *Energy Environ. Sci.* **2014**, *7*, 3061-3068.
[12] B. W. Park, B. Philippe, X. L. Zhang, H. Rensmo, G. Boschloo, E. M. J. Johansson, *Adv. Mater.* **2015**, *27*, 6806-6813.
[13] T. Krishnamoorthy, H. Ding, C. Yan, W. L. Leong, T. Baikie, Z. Y. Zhang, M. Sherburne, S. Li, M. Asta, N. Mathews, S. G. Mhaisalkar, *J. Mater.Chem. A* **2015**, *3*, 23829-23832.
[14] P. P. Sun, Q. S. Li, L. N. Yang, Z. S. Li, *Nanoscale* **2016**, *8*, 1503-1512.
[15] P. P. Sun, Q. S. Li, S. Feng, Z. S. Li, *Phys. Chem. Chem. Phys.* **2016**, *18*, 14408-14418.
[16] W. Shockley, H. J. Queisser, *J. Appl.Phys.* **1961**, *32*, 510.
[17] S. Ruhle, *Solar Energy* **2016**, *130*, 139-147.
[18] Z. Chen, J. J. Wang, Y. Ren, C. Yu, K. Shum, *Appl. Phys.Lett.* **2012**, *101*, 093901.
[19] I. Chung, J. H. Song, J. Im, J. Androulakis, C. D. Malliakas, H. Li, A. J. Freeman, J. T. Kenney, M. G. Kanatzidis, *J. Amer. Chem. Soc.***2012**, *134*, 8579-8587.
[20] P. Xu, S. Y. Chen, H. J. Xiang, X. G. Gong, S. H. Wei, *Chem. Mater.* **2014**, *26*, 6068-6072.
[21] J. Zhang, C. H. Yu, L. L. Wang, Y. Z. Li, Y. H. Ren, K. Shum, *Sci. Rep.* **2014**, *4*, 6954.
[22] I. Chung, B. Lee, J. Q. He, R. P. H. Chang, M. G. Kanatzidis, *Nature* **2012**, *485*, 486-494.
[23] W. J. Yin, J. H. Yang, J. Kang, Y. F. Yan, S. H. Wei, *J. Mater. Chem. A* **2015**, *3*, 8926-8942.
[24] M. B. Price, J. Butkus, T. C. Jellicoe, A. Sadhanala, A. Briane, J. E. Halpert, K. Broch, J. M. Hodgkiss, R. H. Friend, F. Deschler, *Nat. Commun.* **2015**, *6*, 8420.
[25] Y. Yang, D. P. Ostrowski, R. M. France, K. Zhu, J. van de Lagemaat, J. M. Luther, M. C. Beard, *Nat.Photon.* **2016**, *10*, 53-59.
[26] Y. Yamada, T. Yamada, L. Q. Phuong, N. Maruyama, H. Nishimura, A. Wakamiya, Y. Murata, Y. Kanemitsu, *J. Amer. Chem. Soc.* **2015**, *137*, 10456-10459.
[27] H. Wang, K. S. Wong, B. A. Foreman, Z. Y. Yang, G. K. L. Wong, *J.Appl. Phys.* **1998**, *83*, 4773-4776.
[28] W. Y. Nie, H. H. Tsai, R. Asadpour, J. C. Blancon, A. J. Neukirch, G. Gupta, J. J. Crochet, M. Chhowalla, S. Tretiak, M. A. Alam, H. L. Wang, A. D. Mohite, *Science* **2015**, *347*, 522-525.
[29] V. D'Innocenzo, A. R. S. Kandada, M. De Bastiani, M. Gandini, A. Petrozza, *J. Amer.Chem.Soc.***2014**, *136*, 17730-17733.
[30] G. Grancini, S. Marras, M. Prato, C. Giannini, C. Quarti, F. De Angelis, M. De Bastiani, G. E. Eperon, H. J. Snaith, L. Manna, A. Petrozza, *J.Phys. Chem.Lett.* **2014**, *5*, 3836-3842.
[31] Y. Yamada, T. Nakamura, M. Endo, A. Wakamiya, Y. Kanemitsu, *J. Amer. Chem. Soc.* **2014**, *136*, 11610-11613.
[32] G. C. Xing, N. Mathews, S. S. Lim, N. Yantara, X. F. Liu, D. Sabba, M. Gratzel, S. Mhaisalkar, T. C. Sum, *Nat.Mater.* **2014**, *13*, 476-480.
[33] S. D. Stranks, V. M. Burlakov, T. Leijtens, J. M. Ball, A. Goriely, H. J. Snaith. *Phys.Rev.Appl.* **2014**, *2*, 034007.
[34] B. Wu, H. T. Nguyen, Z. Ku, G. Han, D. Giovanni, N. Mathews, H. J. Fan, T. C. Sum, *Adv.Energy Mater.* **2016**, *6*, 1600551.
[35] J. Vaitkus, *Physica Status Solidi A Appl. Res.***1976**, *34*, 769-775.

[36] C. A. Hoffman, K. Jarasiunas, H. J. Gerritsen, A. V. Nurmikko, *Appl. Phys. Lett.* **1978**, *33*, 536-539.
[37] N. Derhacobian, P. Fine, J. T. Walton, Y. K. Wong, C. S. Rossington, P. N. Luke, *Ieee Trans.Nucl.Sci.* **1994**, *41*, 1026-1030.
[38] Y. Rosenwaks, Y. Shapira, D. Huppert, *Phys.Rev. B* **1992**, *45*, 9108-9119.
[39] Y. Yang, Y. Yan, M. J. Yang, S. Choi, K. Zhu, J. M. Luther, M. C. Beard, *Nat.Commun.* **2015**, *6*, 7961.
[40] D. S. Chemla, D. A. B. Miller, P. W. Smith, A. C. Gossard, W. Wiegmann, *Ieee J. Quantum Electron.* **1984**, *20*, 265-275.
[41] A. Le Bris, J. F. Guillemoles, *Appl. Phys. Lett.* **2010**, *97*, 113506.
[42] R. T. Ross, A. J. Nozik, *J. Appl.Phys.* **1982**, *53*, 3813-3818.
[43] T. Tanaka, A. Harata, T. Sawada, *J. Appl. Phys.* **1997**, *82*, 4033-4038.
[44] R. K. Ahrenkiel, J. Dashdorj, *J. Vac. Sci. Technol. B* **2004**, *22*, 2063-2067.
[45] G. J. Rees, *Solid State Electron.* **1985**, *28*, 517-519.
[46] D. Kuciauskas, A. Kanevce, P. Dippo, S. Seyedmohammadi, R. Malik, *Ieee J. Photovolt.* **2015**, *5*, 366-371.
[47] S. M. Beck, J. E. Wessel, *Appl. Phys. Lett.* **1987**, *50*, 149-151.
[48] E. Yablonovitch, D. L. Allara, C. C. Chang, T. Gmitter, T. B. Bright, *Phys. Rev. Lett.* **1986**, *57*, 249-252.
[49] G. C. Xing, B. Wu, S. Chen, J. Chua, N. Yantara, S. Mhaisalkar, N. Mathews, T. C. Sum, *Small* **2015**, *11*, 3606-3613.
[50] G. Xing, N. Mathews, S. Sun, S. S. Lim, Y. M. Lam, M. Graetzel, S. Mhaisalkar, T. C. Sum. *Science* **2013**, *342*, 344-347.
[51] M. I. Saidaminov, A. L. Abdelhady, B. Murali, E. Alarousu, V. M. Burlakov, W. Peng, I. Dursun, L. F. Wang, Y. He, G. Maculan, A. Goriely, T. Wu, O. F. Mohammed, O. M. Bakr, *Nat. Commun.* **2015**, *6*, 7586.
[52] D. Shi, V. Adinolfi, R. Comin, M. J. Yuan, E. Alarousu, A. Buin, Y. Chen, S. Hoogland, A. Rothenberger, K. Katsiev, Y. Losovyj, X. Zhang, P. A. Dowben, O. F. Mohammed, E. H. Sargent, O. M. Bakr, *Science* **2015**, *347*, 519-522.
[53] S. D. Stranks, G. E. Eperon, G. Grancini, C. Menelaou, M. J. P. Alcocer, T. Leijtens, L. M. Herz, A. Petrozza, H. J. Snaith, *Science* **2013**, *342*, 341-344.
[54] M. A. Green, K. Emery, Y. Hishikawa, W. Warta, *Prog. in Photovolt.* **2011**, *19*, 84-92.
[55] C. J. Keavney, V. E. Haven, S. M. Vernon, Emitter structures in MOCVD InP solar cells. *Photovoltaic Specialists Conference, 1990., Conference Record of the Twenty First IEEE* **1990**, *1*, 141-144.
[56] A. B. Sproul, *J. Appl.Phys.* **1994**, *76*, 2851-2854.
[57] G. Xing, M. H. Kumar, W. K. Chong, X. Liu, Y. Cai, H. Ding, M. Asta, M. Grätzel, S. Mhaisalkar, N. Mathews, T. C. Sum, *Adv. Mater.*, DOI: 10.1002/adma.201601418.
[58] A. Wang, J. Zhao, M. A. Green, *Appl.Phys.Lett.* **1990**, *57*, 602-604.
[59] J. S. Huang, Y. C. Shao, Q. F. Dong, *J. Phys.Chem.Lett.* **2015**, *6*, 3218-3227.
[60] K. Vandewal, K. Tvingstedt, A. Gadisa, O. Inganas, J. V. Manca, *Nat.Mater.* **2009**, *8*, 904-909.
[61] M. A. Green, *Solid State Electron.* **1981**, *24*, 788-789.

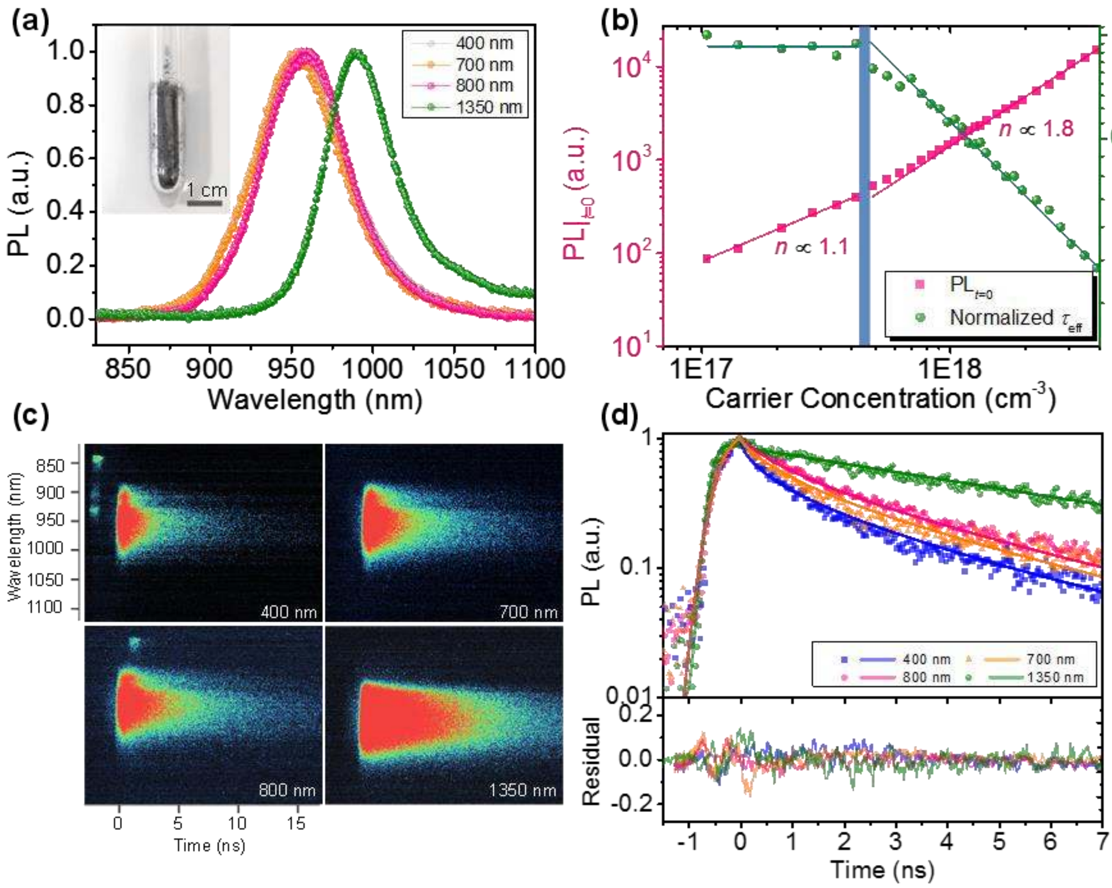

Figure 1. PL properties of $CsSnI_3$ SCs. (a) PL spectra of $CsSnI_3$ with one-photon (400 nm, 700 nm, 800 nm) and two-photon (1350 nm) excitations. Inset: Photograph of $CsSnI_3$ ingot inside an evacuated Pyrex vial. (b) Carrier-concentration dependence of the effective PL lifetime (τ_{eff}) and intensity at t=0 ($PL_{t=0}$). The green solid lines are guides for the eye.(c) Pseudo-color images of TRPL profiles with one-photon and two-photon excitations. (d) Top: PL dynamics with different photoexcitation energies. Solid lines are fits using the model described in the main text. The carrier densities were kept low (<4 $\times 10^{17}$ cm^{-3}) to ensure that first-order recombination dominates. Bottom: fitting residuals.

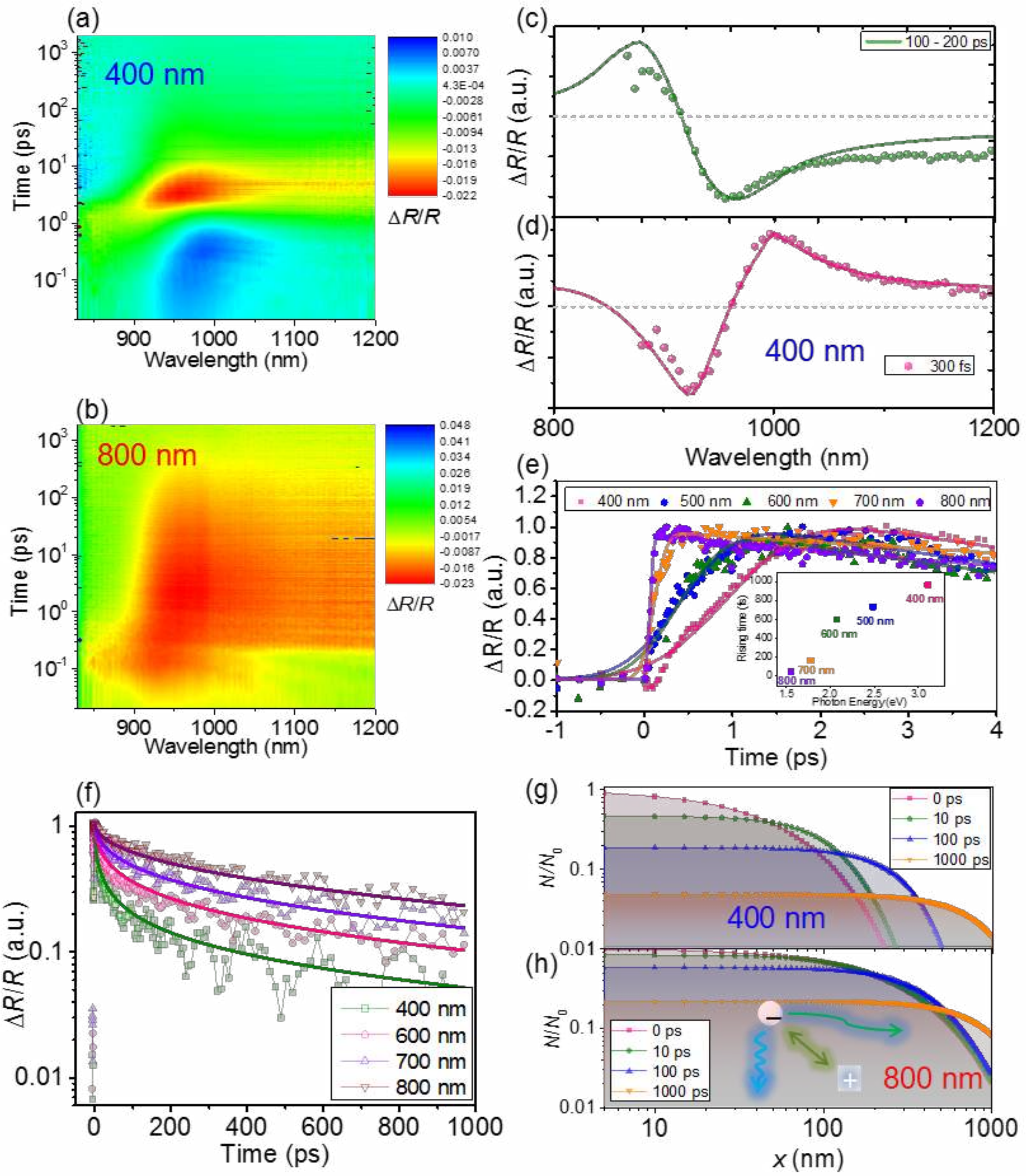

Figure 2. Transient reflection profiles and dynamics of $CsSnI_3$ SCs. The pseudo-color transient reflection profiles of $CsSnI_3$ SC with excitations: (a) 400 nm and (b) 800 nm. (c) TR spectrum after most of the hot-carriers relaxed (*i.e.*, few hundred ps). Both 400 nm and 800 nm excitations show the same TR spectrum profile. (d) TR spectrum at early times (300 fs) when hot-carrier effect and BGR are both present with 400 nm excitation. (e) The rising band-edge TR signal (monitored at 920 nm) following photo-excitation at various wavelengths. Inset: the fitted rise times at different photo-excitation energies. (f) TR decay dynamics are found to accelerate with higher absorbing excitation photons, which can be fitted using a model based on surface recombination and diffusion. Simulated carrier distribution profiles with (g) 400 nm and (h) 800 nm excitations.

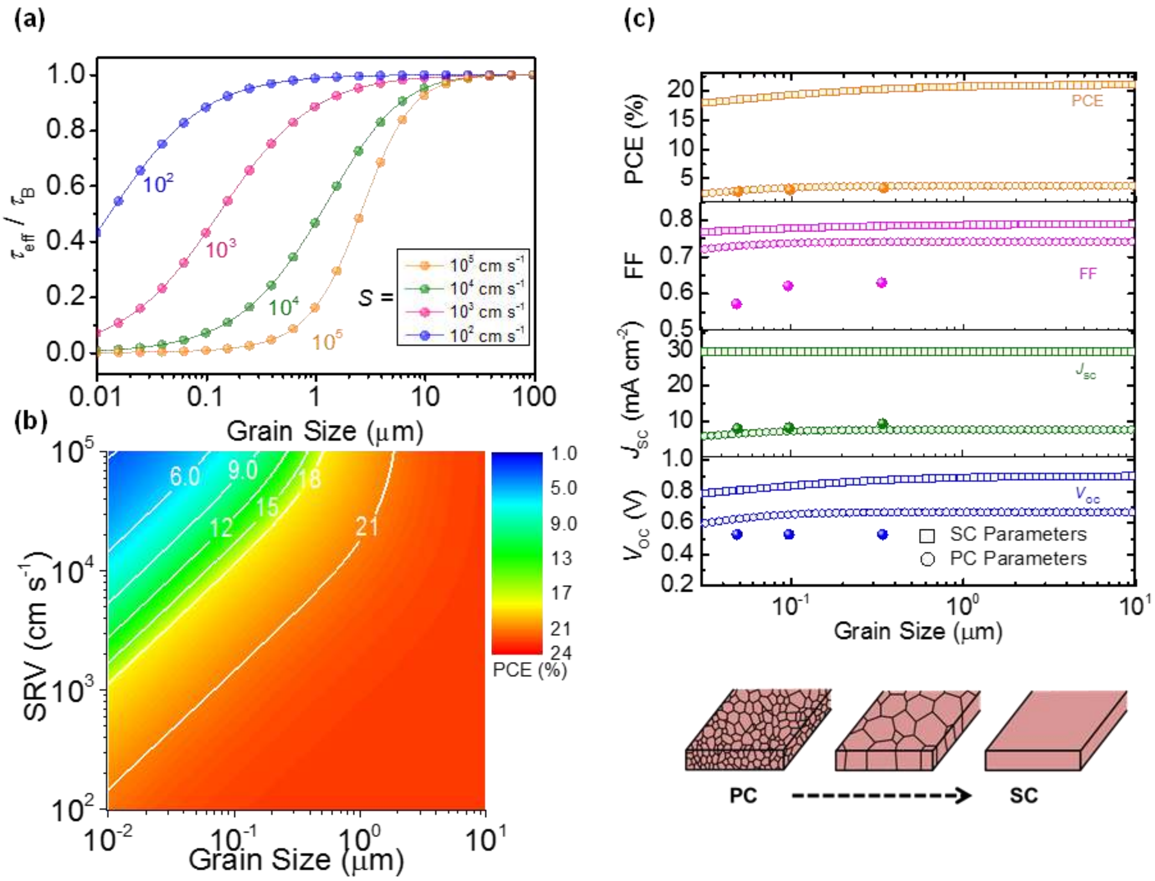

Figure 3. (a) Dependence of the effective carrier lifetime on the grain size and SRV. (b) Pseudo-color simulated PCE and its dependence on SRV and grain size. (c) Prediction of solar cell performance parameters (V_{OC}, J_{SC}, *FF*, and PCE) as a function of grain size using parameters from SCs (thickness: 300 nm) and PCs (thickness: 100 nm). The thicknesses are almost optimized for both cases. Solid circles are experimental data obtained for solar cells based on $CsSnI_3$ polycrystalline thin films without any additives.[5]

Table 1. Comparison of a key properties (*i.e.*, bandgap, PL lifetime, minority carrier diffusion length, doped carrier concentration and surface recombination velocity) that influence the PV performance for $CsSnI_3$ SC, PC, and p-type InP.

	E_g via PL (eV)	τ_{PL} (ns)	$L_{minority\ carrier}$ (nm)	n_{doped} (cm^{-3})	SRV (cm s^{-1})
$CsSnI_3$ SC	1.31	6.6	930	4.5×10^{17}	$< 2 \times 10^3$
$CsSnI_3$ PC	1.34	0.05	16	9.2×10^{18}	
P-type InP	1.35 [38]	4 [38]	1400	5×10^{16} [38]	5×10^2[38]

Pb-free $CsSnI_3$ single crystal possesses superior optoelectronic properties compared to their polycrystalline thin film counterparts for photovoltaic application; uncovered using detailed optical spectroscopy, with a bulk carrier lifetimes of around 6.6 ns, doping concentrations of ~4.5×10^{17} cm^{-3}, minority-carrier diffusion lengths approaching 1 μm and surface recombination velocity of $<2 \times 10^3$ cm s^{-1}.

Keyword Lead-free perovskite crystal, Carrier dynamics, Diffusion length, Surface recombination velocity

Bo Wu, Yuanyuan Zhou, Guichuan Xing, Qiang Xu, Hector F. Garces, Ankur Solanki, Teck Wee Goh, Nitin P. Padture, Tze Chien Sum**

Long Minority-Carrier Diffusion Length and Low Surface-Recombination Velocity in Inorganic Lead-free $CsSnI_3$ Perovskite Crystal for Solar Cells

ToC figure ((Please choose one size: 55 mm broad × 50 mm high **or** 110 mm broad × 20 mm high. Please do not use any other dimensions))

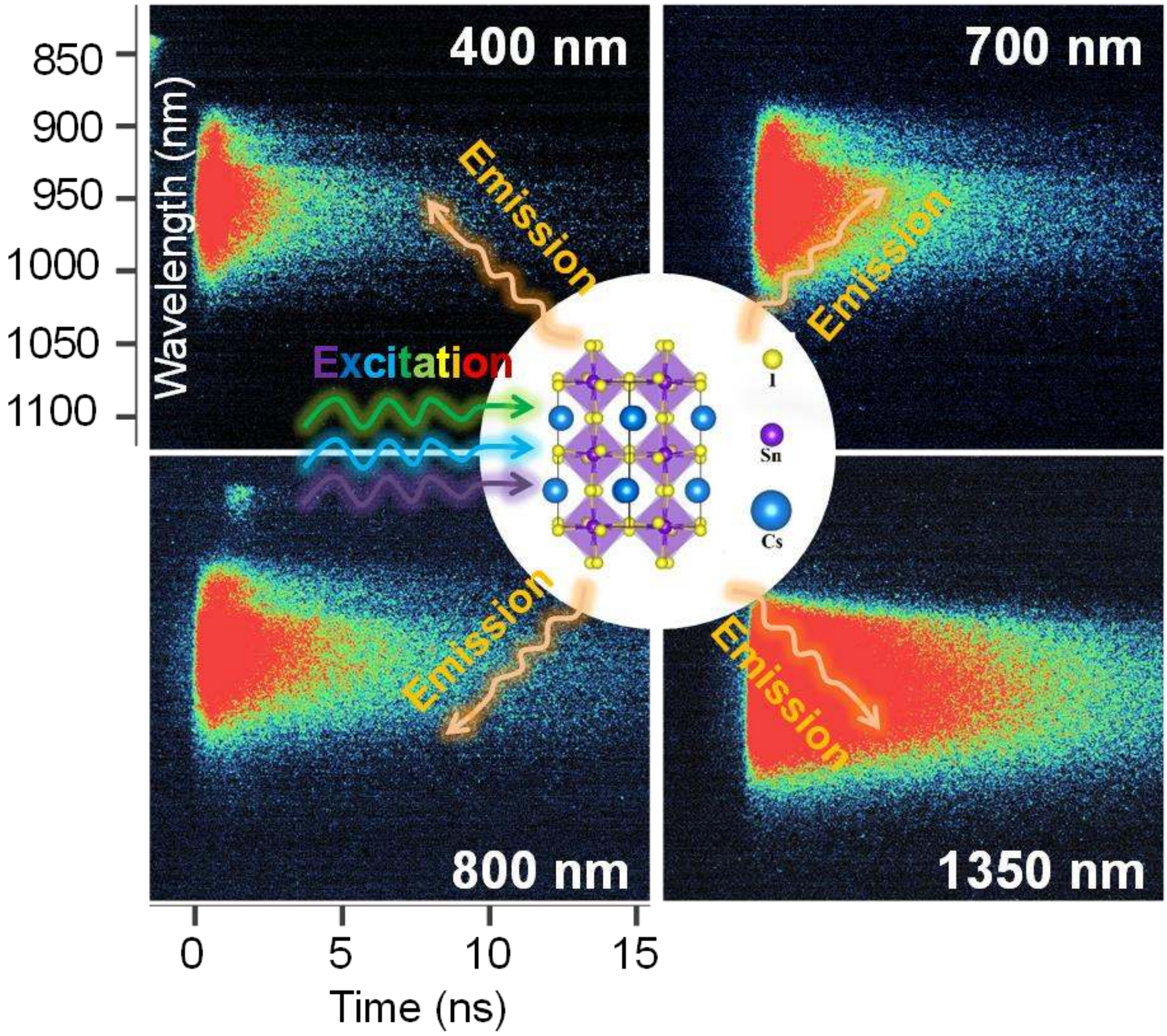

Supporting Information

Long Minority-Carrier Diffusion Length and Low Surface-Recombination Velocity in Inorganic Lead-free $CsSnI_3$ Perovskite Crystal for Solar Cells

Bo Wu, Yuanyuan Zhou, Guichuan Xing, Qiang Xu, Hector F. Garces, Ankur Solanki, Teck Wee Goh, Nitin P. Padture, Tze Chien Sum**

Dr. B. Wu, Dr. G. Xing, Dr. Q. Xu, Mr. A. Solanki, Mr. T.W. Goh, Prof. T.C. Sum, Division of Physics and Applied Physics, School of Physical and Mathematical Sciences, Nanyang Technological University, 21 Nanyang Link, Singapore 637371
Email: Tzechien@ntu.edu.sg
Dr. Y. Zhou, Mr. H.F. Garces, Prof. N.P. Padture, School of Engineering, Brown University, Providence, RI 02912, USA
Email: nitin_padture@brown.edu
Dr. G. Xing, Institute of Applied Physics and Materials Engineering, Faculty of Science and Technology, University of Macau, Macao SAR, China

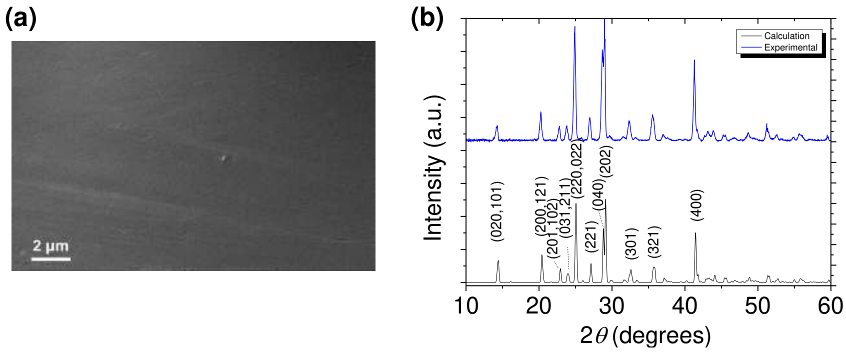

Figure S1. Basic properties of $CsSnI_3$ SCs. (a) SEM image of melt-synthesized $CsSnI_3$ ingot showing very smooth, grain-boundary free surface. (b) Experimentally measured and theoretically-predicted XRD patterns from crushed $CsSnI_3$ ingot powder.

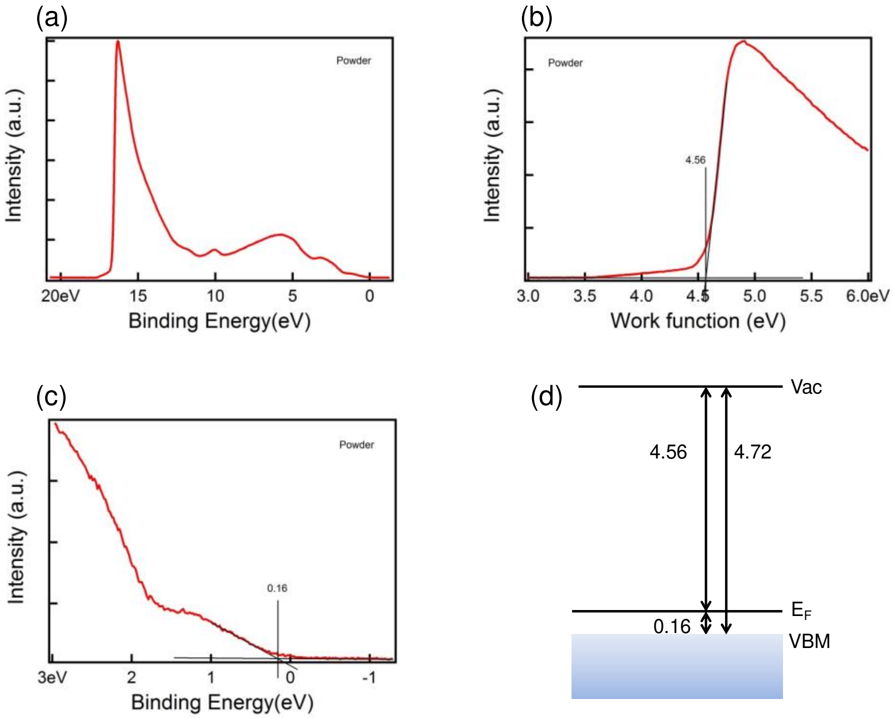

Figure S2. UV photoemission spectroscopy (UPS) data of $CsSnI_3$ SCs. (a) UPS data of the $CsSnI_3$ SCs, from which the Fermi-level and VBM positions are obtained and as shown in (b) and (c). (d) Energy levels of the $CsSnI_3$ SCs.

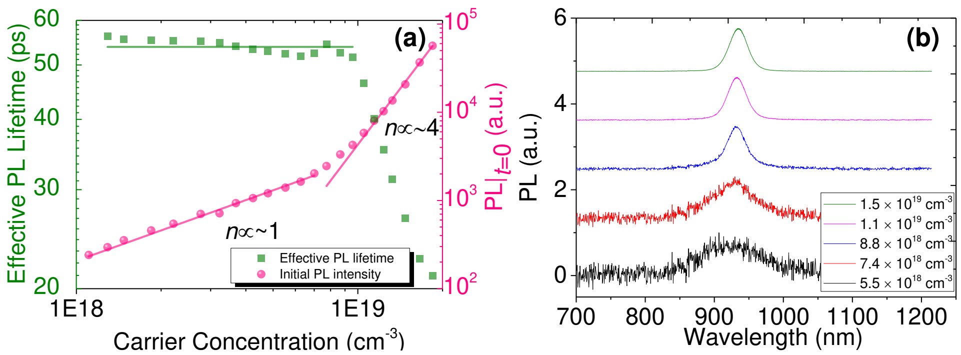

Figure S3. PL properties of solution-processed $CsSnI_3$ polycrystalline thin film. (a) Carrier-concentration dependent effective PL lifetimes and intensity at *t*=0. (b) ASE is observed at the recombination-order transition point in (a), indicating that the thin films goes from recombination with doped carriers/deep defects directly to ASE after filling up these defects.

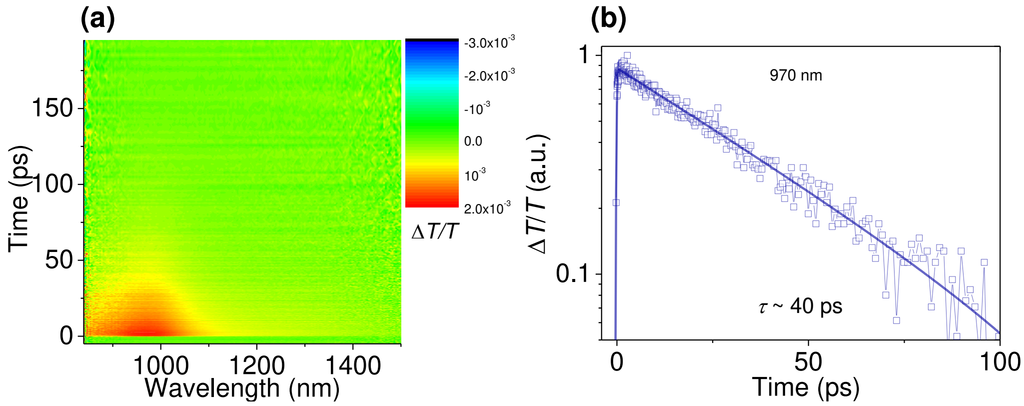

Figure S4. TA profile and dynamics of solution-processed $CsSnI_3$ polycrystalline thin film. (a) Pseudo-color TA profile of $CsSnI_3$ thin film with 800 nm excitation (~30 μJ cm^{-2}). (c) Photobleaching decay dynamics probed at 970 nm show a decay time constant of 40±1 ps.

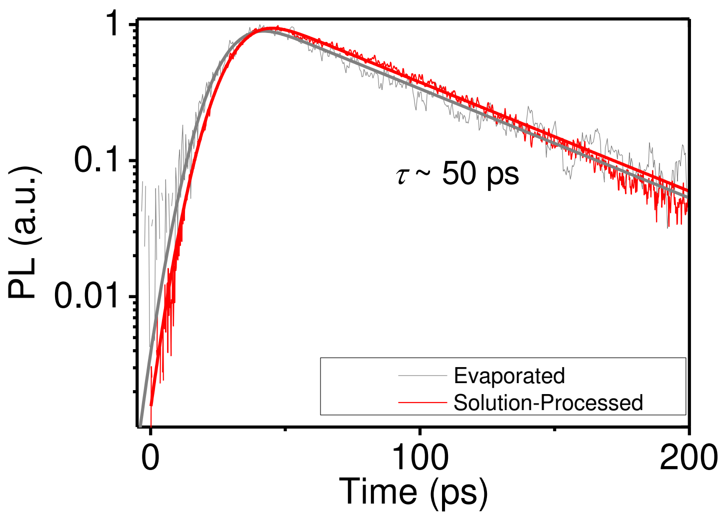

Figure S5. PL dynamics of $CsSnI_3$ polycrystalline thin film deposited by solution and evaporation methods. Both films show similar and consistently short lifetimes of around 50 ps.

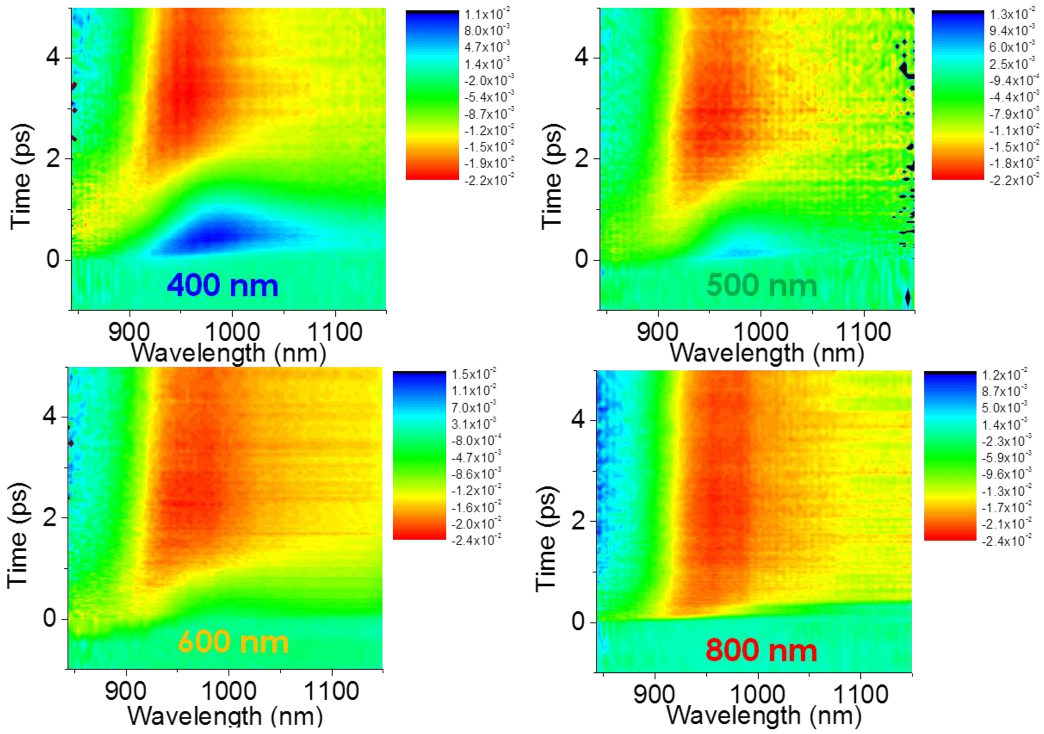

Figure S6. Pseudo-color TR profiles of $CsSnI_3$ SCs at early delay times (< 5 ps). Pump photon energies used are: (a) 400 nm (b) 500 nm (c) 600 nm, and (d) 800 nm.

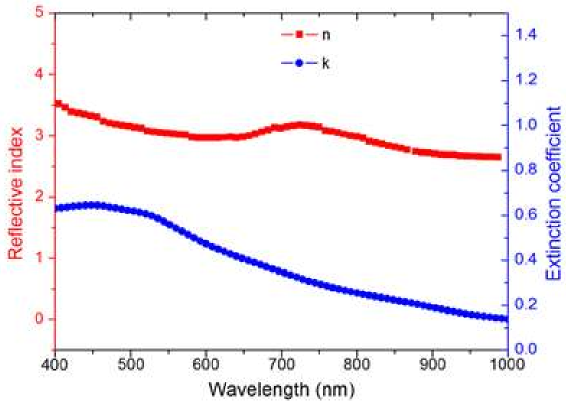

Figure S7. Refractive index (*n*) and extinction coefficient (*k*) of $CsSnI_3$ polycrystalline thin film characterized using ellipsometry (VB250, VASE, J. A. Woollam, USA). Quartz substrates were used for all the optical measurements.

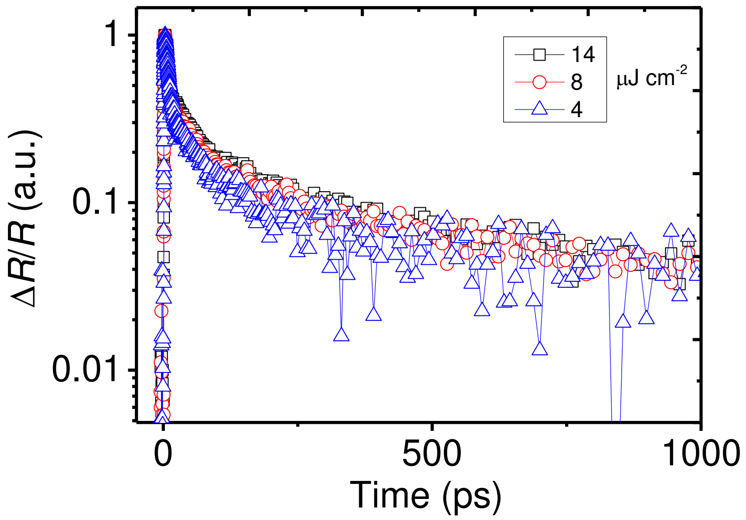

Figure S8. TR dynamics of $CsSnI_3$ SC with 400 nm photoexcitation using various pump fluence. The influence of carrier concentration on the reflection dynamics is not significant. To avoid measuring ambipolar carrier diffusion rather than minority carrier diffusion, we performed the experiments at low pump fluence to minimize the carrier concentrations.

Calculation of the electronic structure of $CsSnI_3$ bulk and (001) surfaces.

We employ the all-electron-like projector augmented wave (PAW) method[1] and the Perdew-Burke-Ernzerhof revised for solids (PBEsol) exchange correlation potential[2] as implemented in the VASP code.[3] In the basis, the semicores of Cs and Sn atoms are treated as valence electrons, *i.e.*, 9 valence electrons for Cs ($5s^2 5p^6 6s^1$) atom and 14 valence electrons for Sn ($4d^{10} 5s^2 5p^2$) atom. The cut-off energy for the plane wave expansion of the wave functions is 500eV. All atoms are fully relaxed. The Hellman-Feynman forces are less than of 0.01 eV/Å. The 3×3×1 Monkhorst-Pack grid of k-points[4] for Brillouin zone integration was used in the calculations of structure relaxation. For their electronic structures calculations, the double Monkhorst-Pack grid of k-points is used. In the calculations, the primitive unit cell of $CsSnI_3$ is orthorhombic with space group Pnma (D_{2h}^{16}). Their optimized lattice parameters are listed in the **Table S1**. For the (0 0 1) $CsSnI_3$ surface structure, it includes two different terminated surfaces, *i.e.*, CsI and SnI surface. In order to make the surface models to be non-polarized, we build two (0 0 1) surface structures with CsI and SnI terminated surfaces, respectively. The vacuum thickness for both surface structures are of 20 Å. The optimized structures are shown in Fig. S9. The calculated surface energies of the two slab models are list in **Table S2**, which show that the slab terminate by two CsI surfaces are favorable because of its lower surface energy.

Table S1. The optimized lattice parameters. The values in brackets are experimental data.

	a_0 (Å)	b_0 (Å)	c_0 (Å)
This work	8.60	8.56	12.24
Exp. Value[6]	8.69	8.64	12.38

As shown in Figure S9a, the calculated band gap of bulk $CsSnI_3$ is 0.45 eV, which is smaller than experimental value. This is because the calculations based on density functional theory (DFT) strongly underestimated the band gap. Nonetheless, the calculated results are similar with other calculation works.[7] In Fig. S9b and S9c, we showed the band structures of (0 0 1) $CsSnI_3$ slabs. We found that both surface structures have the same band gap. The band gap of the slabs are larger than that of bulk $CsSnI_3$ and the surface states do not appear in the band gaps.

Table S2. The calculated surface energies σ.

	SnI surface	CsI surface
σ (meV/Å^2)	8.72	2.44

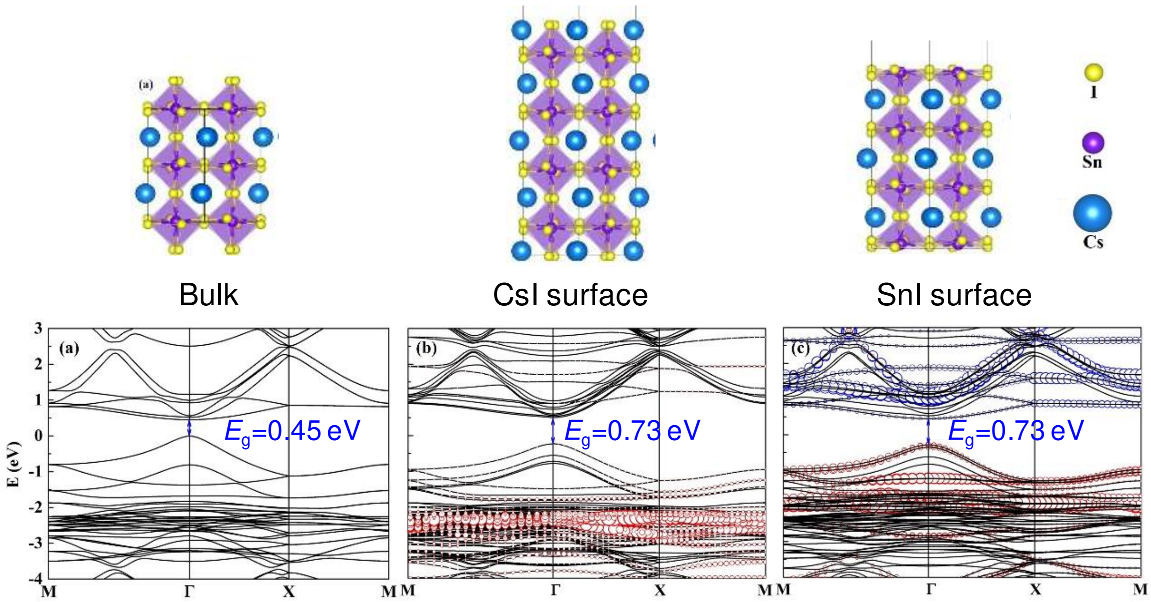

Figure S9. Calculated band structure of $CsSnI_3$ bulk and its (0 0 1) surfaces. The band structures of (a) bulk $CsSnI_3$, (0 0 1) $CsSnI_3$ slab with (b) terminated by CsI surface and (c) terminated by SnI surface. The blue and red circles present the components of 5p states of Sn and I atoms at the surface, respectively. The size of the circles are representative of the weights of the components.

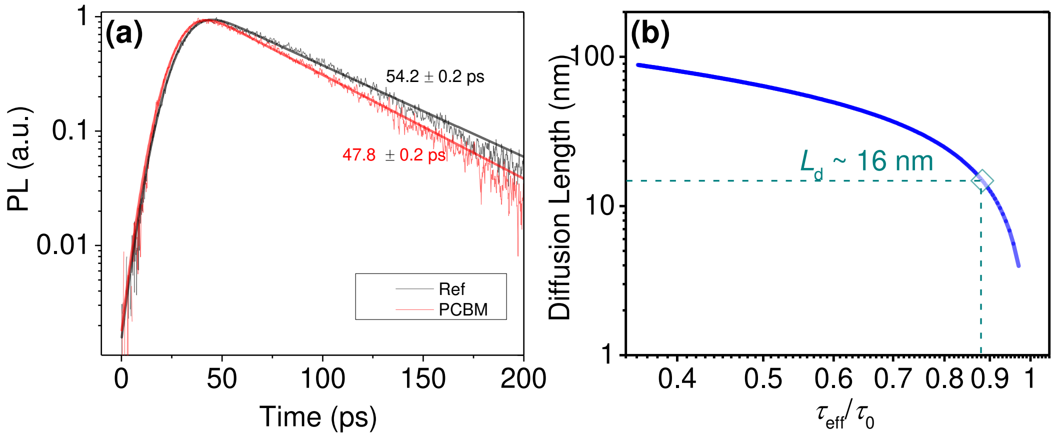

Figure S10. Minority carrier diffusion length in $CsSnI_3$ thin films. (a) PL dynamics for a 120 nm thick $CsSnI_3$ polycrystalline thin film with and without a PCBM layer on top. The PCBM layer was used to extract the minority carriers of $CsSnI_3$ (electrons). (b) Diffusion length vs. the lifetime ratio with and without PCBM layer. The diffusion length of ~16 nm was determined from experiments.

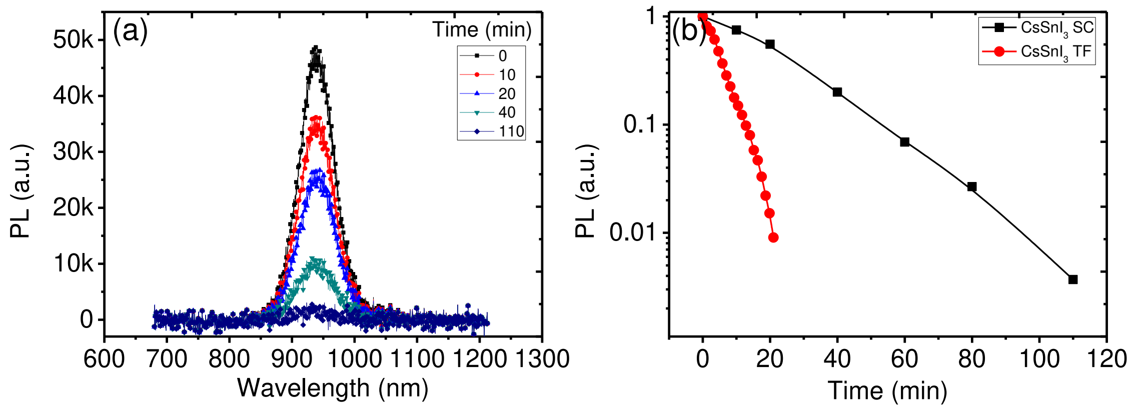

Figure S11. PL degradation study of $CsSnI_3$ single crystal. (a) PL spectra evolution with time. (b) Quenching of the peak PL intensity with time for single crystal and thin film. The degradation study was performed at 20°C, 60% humidity and under continuous illumination of 800 nm fs-pulses (>8.5 μJ cm^{-2}).

Calculation of the theoretical solar cell performance parameters.

The short-circuit current density (J_{SC}) is mainly limited by the minority carrier drift and diffusion. $J_{SC}=J_{drift}+J_{diffuse}$, where J_{drift} is the drift current in the depletion layer due to the presence of build-in field, and $J_{diffuse}$ is the diffusion current out of the depletion layer (**Figure S9**).

$$J_{\text{drift}} = qG\int_0^W \exp(-x/L_{\text{drift}})dx = qGL_{\text{drift}}(1-\exp(-W/L_{\text{drift}})) , \quad (1)$$

where W is the depletion width, G is the carrier concentration, L_{drift} is the carrier drift length $L_{drift} \sim \mu E\tau = \mu\tau V_{bi}/W$, V_{bi} is the build-in field (~ 1V), μ is the effective carrier mobility, τ is the effective carrier lifetime.

$$J_{\text{diffuse}} = qD\frac{\partial\Delta n(x)}{\partial x}\bigg|_{x=W} \exp(-\frac{W}{L_{\text{drift}}}) = qG\frac{L_{\text{drift}}L_{\text{diffuse}}}{L_{\text{drift}}+L_{\text{diffuse}}}\exp(\frac{-W}{L_{\text{drift}}}) , \quad (2)$$

where $L_{\text{diffuse}} = \sqrt{D\tau}$, D is the effective diffusion coefficient.[8]

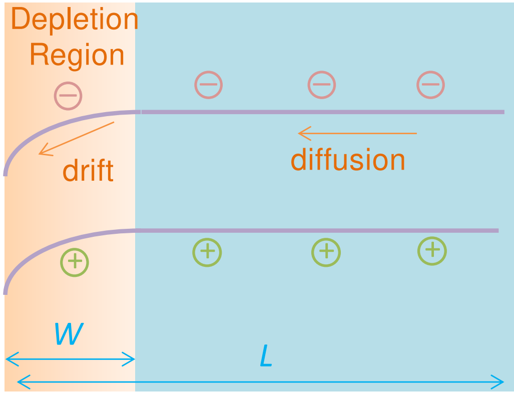

Figure S12. Schematic of the drift and diffusion of excess carriers.

References

1. P. E. Blöchl, Phys. Rev. B **50**, 17953 (1994).
2. J. P. Perdew, A. Ruzsinszky, G. I. Csonka, O. A. Vydrov, G.E. Scuseria, L. A. Constantin, X. Zhou, and K. Burke, Phys. Rev. Lett. **100**, 136406 (2008).
3. G. Kresse and J. Furthmuller, Phys. Rev. B **54**, 11169 (1996).
4. H. J. Monkhorst and J. D. Pack, Phys. Rev. B **13**, 5188 (1976).
5. D. T. Cromer and K. Herrington, J. Am. Chem. Soc. **77**, 4708 (1955).
6. K. Yamada, S. Funabiki, H. Horimoto, T. Matsui, T. Okuda, and S. Ichiba, Chem. Lett. **20**, 801 (1991).
7. I. Borriello, G. Cantele, and D. Ninno, Phys. Rev. B **77**, 235214 (2008).
8. L. Singh and M. Bhatnagar, Short circuit current variation of GIGS solar cells with grain boundaries recombination velocity. Indian J Pure Ap Phy 42, 841-844 (2004).